Thermoelastic analysis of a geological repository with distributed decay heat sources by the image method in combination with a numerical integration scheme

Dongdong Liu[1,*], *Yanyong* Xiang[1]

[1] School of Civil Engineering, Beijing Jiaotong University, Beijing 100044, People's Republic of China

Abstract: The disposal of nuclear waste involves thermo-mechanical reaction of the host rock to the buried waste – a distributed heat source that decays. To solve the problem within the half infinite space confined by the ground surface, an image method is developed. Specifically, a negative image of the heat source with the ground surface as the mirror, i.e. a mirrored heat sink is utilized so that the normal traction generated by the heat source can be counterbalanced, and a numerical scheme of integration of the classical Cerruti solution is developed to include the effect of tangential shear traction on the ground surface caused by the heat sources and their mirrored sinks. For a conceptual repository model, large thermal shear stress, tensile stress, and deformation occur at the corner, between adjacent drifts, and at the boundary of the repository area, respectively. For a prescribed thermal loading, it is more efficient to mitigate the thermo-mechanical effects through enlarging the pit spacing than increasing the drift spacing.

1 Introduction

Due to the radioactivity and toxicity of nuclear waste, a final disposal solution is required for a sustainable nuclear power program[1]. Constructing geological repositories is currently recommended as a feasible and reliable option to safely isolate radionuclides from the biosphere for very long time. For example, the Swedish Nuclear Fuel and Waste Management Company has submitted permit applications for the construction of a final repository in crystalline bedrock[2].

In the design of a geologic repository, the thermo-mechanical interaction induced by heat emitted from nuclear waste is a major factor. The heat can change the temperature field and create thermal stress in surrounding rocks[3]. The thermal stress may cause rock fractures increasing the possibility of groundwater intrusion into storage area[4]. The salt in groundwater may corrode the cylindrical container made up of copper or cast iron. Meanwhile, the high temperature environment can promote this corrosion process[5]. Once containers are damaged, radionuclides may quickly reach the ecosystem by groundwater flowing through fractures. To evaluate the safety of a potential repository, the coupled thermo-mechanical process is of interest.

Crystalline, as one kind of candidate rocks, has very low permeability. Thus heat propagates mainly by conduction in a geologic repository. Several appropriate local-scale models are developed to investigate the heat transfer or thermo-mechanical interaction around the central canister[6-16]. Although multiple barriers consisting of the container, buff, backfill and rock can be considered, these local-scale models are only available for the symmetrical position at any time scale or asymmetrical region at short-term scale. Designing a repository also needs some large-scale models which are capable of describing the variations of temperature and thermal stress at any location in the repository during the long-term disposal period. Mapping the canister on a rectangular plane, point or line, authors proposed several analytical or semi-analytical models for the repository-scale heat transfer analysis[17-20]. Analytical[21] and regional numerical methods[22] are also adopted to analyze the repository-scale thermo-mechanical interaction based on the plane model. But, large errors of thermal stress-displacement exist near the disposal area on account to the significant geometric difference between the cylindrical canister and the rectangular plane. Therefore, a more efficient repository-scale model is of requirement for the thermo-mechanical assessment.

In the present paper, the thermal loading of a nuclear waste repsoitory is simplified into distrbuted and decaying line heat sources. To satisfy the constant temperature and stress-free bounday conditions at the ground surface, an image method in cobination with a numerical integration scheme is developed. The method is first comapred with existent lierature, and then applied to some hypothetical situations to examine the thermo-mechnical effects.

2 Mathematical equations

Fig.1 illustrates a schematic of the KBS-3V repository [23]. In this study, the crystalline is assumed as a semi-infinite, isothermal, homogeneous, elastic medium.

* Corresponding author: dond_liu@126.com

Temperature-independent rock properties, uniform initial temperature field, constant ground surface temperature and rectangular disposal region are postulated as well.

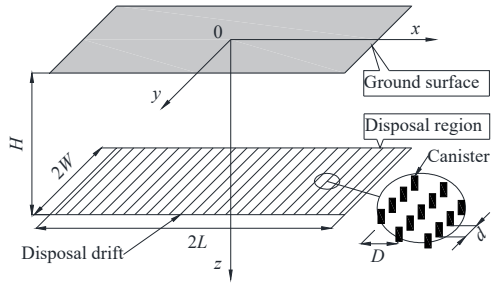

Fig. 1. Schematic of a repository (*H*, 2*L*, 2*W* repository depth length, width, respectively; *d*, pit spacing; *D*, drift spacing)

2.1 Energy conversation equation

The heat propagation is dominated by conduction due to the low permeability of crystalline. The energy conversation equation is

$$\lambda\theta_{,ii}-\rho c\dot{\theta}=0 \tag{1}$$

where θ is the temperature increment; ρ rock density; λ rock thermal conductivity; c rock specific heat; $i= x, y, z$; the subscript comma indicates partial differential; the superscript point represents the derivative of time t.

2.2 Equilibrium equation

In the absence of body force, the equilibrium equation is

$$\sigma_{ij,i}=0 \tag{2}$$

where σ_{ij} is the stress tensor; $j= x, y, z$.

Under the non-isothermal condition, the constitutive equation is

$$\sigma_{ij}=2G\varepsilon_{ij}+2G\delta_{ij}\left[\frac{\upsilon}{1-2\upsilon}\varepsilon_v-\frac{\alpha(1+\upsilon)}{1-2\upsilon}\theta\right] \tag{3}$$

where $\varepsilon_{ij}=(u_{i,j}+u_{j,i})/2$ is the strain tensor, u_i the displacement in i-direction; $\varepsilon_v=\varepsilon_{xx}+\varepsilon_{yy}+\varepsilon_{zz}$ volumetric strain; G shear modulus; υ Poison's ratio; $\alpha=\lambda/\rho c$ thermal expansion coefficient; δ_{ij} Kronecker delta function.

Substituting Eq.(3) in Eq.(2) yields[24]

$$(1-2\upsilon)u_{i,jj}+\varepsilon_{v,i}-2\alpha(1+\upsilon)\theta_{,i}=0 \tag{4}$$

2.3 Initial and boundary conditions

The following initial and boundary conditions are used.

$$\theta\big|_{t=0}=\theta\big|_{z=0}=\theta\big|_{\boldsymbol{x}\to\infty}=0 \tag{5}$$

$$u_i\big|_{t=0}=u_i\big|_{\boldsymbol{x}\to\infty}=0 \tag{6}$$

$$\sigma_{ij}\big|_{t=0}=\sigma_{ij}\big|_{z=0}=0 \tag{7}$$

where the superscript $\boldsymbol{x}= (x, y, z)$.

3 Solution for decay heat sources

3.1 Solution for an infinite space

Due to an instantaneous unit point heat source in the infinite region, Carslaw et al. [25] gave the temperature solution which met the Eqs.(1) and (5) except for the temperature boundary condition. Using the temperature solution, Dargush et al. [26] derived the thermoelastic solution which satisfied the Eqs.(2), (3), (4), (6) and (7) except for the stress boundary condition. Integrating the thermoelastic solution with respect to time, we obtain the thermal displacement u^{ch} and stress σ^{ch} induced by a constant unit point heat source at point $\boldsymbol{x}'$ and time t_0.

$$u_i^{\mathrm{ch}}(\boldsymbol{x}-\boldsymbol{x}',t-t_0)=\frac{\beta(x_i-x'_i)}{8\pi\rho cR}\left[\operatorname{erfc}(\zeta_0)+\frac{\operatorname{erf}(\zeta_0)}{2\zeta_0^2}-\frac{\exp(-\zeta_0^2)}{\pi^{1/2}\zeta_0}\right] \tag{8a}$$

$$\sigma_{ij}^{\mathrm{ch}}(\boldsymbol{x}-\boldsymbol{x}',t-t_0)=\frac{\beta G}{4\pi\rho cR}\left\{\delta_{ij}\left[\frac{\operatorname{erf}(\zeta_0)}{2\zeta_0^2}-\frac{\exp(-\zeta_0^2)}{\pi^{1/2}}-\operatorname{erfc}(\zeta_0)\right]-\frac{(x_i-x'_i)(x_j-x'_j)}{R^2}\left[\frac{3\operatorname{erf}(\zeta_0)}{2\zeta_0^2}-\frac{3\exp(-\zeta_0^2)}{\pi^{1/2}}+\operatorname{erfc}(\zeta_0)\right]\right\} \tag{8b}$$

where $\beta=\alpha(1+\upsilon)/(1-\upsilon)$; $\zeta_0=R/\sqrt{4\alpha(t-t_0)}$ in which $R=\sqrt{(x-x')^2+(y-y')^2+(z-z')^2}$.

With regard to a time varying point heat source, we divided the period t_0-t into intervals of N. The heat source strength is assumed to be constant and equal to $Q(t_n)$ during the n^{th} time lag. Based on the solutions in Eq.(8), the thermal displacement $\bar{u}$ and stress $\bar{\sigma}$ are

$$\bar{u}_i(\boldsymbol{x}-\boldsymbol{x}',t)=\sum_{n=1}^{N}Q(t_n)\left[u_i^{\mathrm{ch}}(\boldsymbol{x}-\boldsymbol{x}',t-t_{n-1})-u_i^{\mathrm{ch}}(\boldsymbol{x}-\boldsymbol{x}',t-t_n)\right] \tag{9a}$$

$$\bar{\sigma}_{ij}(\boldsymbol{x}-\boldsymbol{x}',t)=\sum_{n=1}^{N}Q(t_n)\left[\sigma_{ij}^{\mathrm{ch}}(\boldsymbol{x}-\boldsymbol{x}',t-t_{n-1})-\sigma_{ij}^{\mathrm{ch}}(\boldsymbol{x}-\boldsymbol{x}',t-t_n)\right] \tag{9b}$$

3.2 Solution for a semi-infinite space

Except for σ_{yz} and σ_{zx} at the ground surface, other boundary conditions are satisfied by adding the effect of a heat sink with equal magnitude at point (x', y', $-z'$). However, these two shear stresses caused by the heat source are the same as ones resulted by the heat sink, respectively. Therefore, the solution of the following stress boundary problem should be superimposed.

$$f_x(t) = -2\bar{\sigma}_{zx}(t)\big|_{z=0};\ f_y(t) = -2\bar{\sigma}_{yz}(t)\big|_{z=0} \tag{10}$$

For the tangential force on a half-space sufrace, the theoretical solutions were found by Cerruti. The generalized integrals of the Cerruti solutions related to the load in x-direction are

$$\bar{\bar{u}}_x^x(\boldsymbol{x}) = \frac{1}{4\pi G}\Big[2(1-\upsilon)(x-\xi)\ln(r+y-\eta) + 2(y-\eta)\cdot\ln(r+x-\xi) + z^2(\Lambda_1+\Lambda_2) - (1-2\upsilon)(x-\xi)z\Lambda_3\Big] \tag{11a}$$

$$\bar{\bar{u}}_y^x(\boldsymbol{x}) = -\frac{1}{4\pi G}\Big[2\upsilon r + (1-2\upsilon)z\ln(r+z)\Big] \tag{11b}$$

$$\bar{\bar{u}}_z^x(\boldsymbol{x}) = \frac{1}{4\pi G}\Big\{(1-2\upsilon)\Big[(y-\eta)\ln(r+z) + (x-\xi)^2\Lambda_3\Big] - 2\upsilon z\ln(r+y-\eta)\Big\} \tag{11c}$$

$$\bar{\bar{\sigma}}_{xx}^x(\boldsymbol{x}) = -\frac{1}{2\pi}\left\{\frac{(1-2\upsilon)rz^2 - (z+2\upsilon r)(x-\xi)^2}{r(r+z)\left[(x-\xi)^2+z^2\right]}(y-\eta) - 2\ln(r+y-\eta)\right\} \tag{11d}$$

$$\bar{\bar{\sigma}}_{yy}^x(\boldsymbol{x}) = -\frac{1}{2\pi}\left[\frac{z+2\upsilon r}{r(r+z)}(y-\eta) - 2\upsilon\ln(r+y-\eta)\right] \tag{11e}$$

$$\bar{\bar{\sigma}}_{zz}^x(\boldsymbol{x}) = \frac{(y-\eta)z^2}{2\pi r\left[(x-\xi)^2+z^2\right]} \tag{11f}$$

$$\bar{\bar{\sigma}}_{xy}^x(\boldsymbol{x}) = -\frac{1}{2\pi}\left[\frac{z+2\upsilon r}{r(r+z)}(x-\xi) - 2\ln(r+x-\xi)\right] \tag{11g}$$

$$\bar{\bar{\sigma}}_{yz}^x(\boldsymbol{x}) = -\frac{z}{2\pi r} \tag{11h}$$

$$\bar{\bar{\sigma}}_{zx}^x(\boldsymbol{x}) = -\frac{1}{2\pi}\left\{\arctan\left[\frac{(x-\xi)(y-\eta)}{rz}\right] - \frac{(x-\xi)(y-\eta)z}{r\left[(x-\xi)^2+z^2\right]}\right\} \tag{11i}$$

where the superscript denotes the load direction; ξ and η denote the boundary coordinates, and are parallel with x- and y-axis, respectively; $r = \sqrt{(x-\xi)^2+(y-\eta)^2+z^2}$;

$$\Lambda_1 = \frac{1}{|z|}\left\{\frac{\pi}{2} - \arcsin\left[\frac{(x-\xi)^2 + r(x-\xi) + z^2}{(r+x-\xi)\sqrt{(x-\xi)^2+z^2}}\right]\right\};$$

$$\Lambda_2 = \frac{1}{|z|}\left\{\frac{\pi}{2} - \arcsin\left[\frac{(y-\eta)^2 + r(y-\eta) + z^2}{(r+y-\eta)\sqrt{(y-\eta)^2+z^2}}\right]\right\};$$

$$\Lambda_3 = \frac{1}{|x-\xi|}\left\{\frac{\pi}{2} - \arcsin\left[\frac{(x-\xi)^2 + rz + z^2}{(r+z)\sqrt{(x-\xi)^2+z^2}}\right]\right\}.$$

The improper integrals of the Cerruti solutions, related to the y-direction force can be calculated by using the abbove approach. The ground surface is discretized by rectangles of S. Assuming uniform load over each element, combining Eqs.(10) and (11) yields

$$\bar{\bar{u}}_i^*(\boldsymbol{x},t) = \sum_{s=1}^{S}\Big[f_{sx}^{\mathrm{c}}(t)\bar{\bar{u}}_i^x(\boldsymbol{x}) + f_{sy}^{\mathrm{c}}(t)\bar{\bar{u}}_i^y(\boldsymbol{x})\Big]\Big|_{\xi_{s1}}^{\xi_{s2}}\Big|_{\eta_{s1}}^{\eta_{s2}} \tag{12a}$$

$$\bar{\bar{\sigma}}_{ij}^*(\boldsymbol{x},t) = \sum_{s=1}^{S}\Big[f_{sx}^{\mathrm{c}}(t)\bar{\bar{\sigma}}_{ij}^x(\boldsymbol{x}) + f_{sy}^{\mathrm{c}}(t)\bar{\bar{\sigma}}_{ij}^y(\boldsymbol{x})\Big]\Big|_{\xi_{s1}}^{\xi_{s2}}\Big|_{\eta_{s1}}^{\eta_{s2}} \tag{12b}$$

where s denotes the s^{th} element; f_{sx}^{c} and f_{sy}^{c} the values of f_x and f_y at the element center, respectively; ξ_{s1} and ξ_{s2} the region limits of the element in x-direction; η_{s1} and η_{s2} the region limits of the rectangle in y-direction.

If z=0, the deformation formula Eq.(12a) is equal to that[27]. By Eqs.(9) and (12), the thermal displacement and stress of a semi-infinite space are

$$u_i^*(\boldsymbol{x},t) = \bar{u}_i(\boldsymbol{x}-\boldsymbol{x}',t) - \bar{u}_i(\boldsymbol{x}-\boldsymbol{x}'',t) + \bar{\bar{u}}_i^*(\boldsymbol{x},t) \tag{13a}$$

$$\sigma_{ij}^*(\boldsymbol{x},t) = \bar{\sigma}_{ij}(\boldsymbol{x}-\boldsymbol{x}',t) - \bar{\sigma}_{ij}(\boldsymbol{x}-\boldsymbol{x}'',t) + \bar{\bar{\sigma}}_{ij}^*(\boldsymbol{x},t) \tag{13b}$$

where $\boldsymbol{x}''$= (x', y',$-z'$).

The abbove results are applied to derive the solutions for multiple line heat sources. Among heat sources of M, the m^{th} one with a strength of $Q_m(t)$ is L_m high and evenly divided into K_m segments. The k^{th} segment approximates to a point with the Simpson's weight of w_k. The Simpson's weights are[28]

$$[w_1, w_2, \cdots, w_K] = \left[\frac{3}{8}, \frac{7}{6}, \frac{23}{24}, 1, \cdots 1, \frac{23}{24}, \frac{7}{6}, \frac{3}{8}\right] \tag{14}$$

The thermoelastic induced by all heat sources are

$$u_i(\boldsymbol{x},t) = \sum_{m=1}^{M}\sum_{k=1}^{K_m} w_k u_i^*(\boldsymbol{x},t) \tag{15a}$$

$$\sigma_{ij}(\boldsymbol{x},t) = \sum_{m=1}^{M}\sum_{k=1}^{K_m} w_k \sigma_{ij}^*(\boldsymbol{x},t) \tag{15b}$$

4 Validation and application

4.1 Repository layout

The heat released by per canister is[18]

$$Q(t)=1547\left[0.070\exp(-0.05t)+0.713\exp(-0.02t)\right.$$
$$-0.051\exp(-0.005t)+0.231\exp(-0.002t)$$
$$+0.024\exp(-0.0005t)-0.009\exp(-0.0002t)$$
$$\left.+0.002\exp(-0.0005t)\right] \quad (16)$$

where the unit of t is year.

Some parameters are listed in Table 1[18].

Table 1. Calculation parameters[18]

Parameter	Value	Parameter	Value
Density (kg·m^{-3})	2600	Poisson's ratio	0.25
Specific heat (J·kg^{-1}·°C^{-1})	800	Shear modulus (GPa)	15
Conductivity (W·m^{-1}·°C^{-1})	3.0	Thermal expansion coefficient (°C^{-1})	8×10^{-6}
Repository depth (m)	500	Repository width (m)	960
Pit spacing (m)	5	Drift spacing (m)	48
Drift length (m)	1000	Canister number	4000
Canister height (m)	4.8	Canister radius (m)	0.525

4.2 Model comparison

The present model is compared with the one[21] which applies the planar heat source model and neglects the stress-free condition at the ground surface. The line $\bar{L}$ (z_1=472m, z_2=497m) shown in Fig.2 is selected for examination of the comparison.

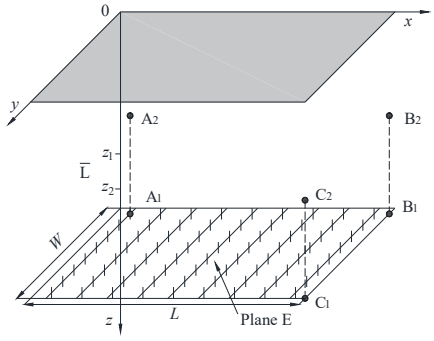

Fig. 2. Illsutration of one line, one plane, and six points for examination of the calculation results.

Fig.3 illustrates the thermal effects along line $\bar{L}$ after 10 years of closure. The compressive stress is defined positive while tensile stress negative. Good agreements can be found between the two solutions when the distance from the examination point to the central canister center exceeds 25m. But as the distance decreases, large differences of the two solutions can be observed due to the different heat source model used.

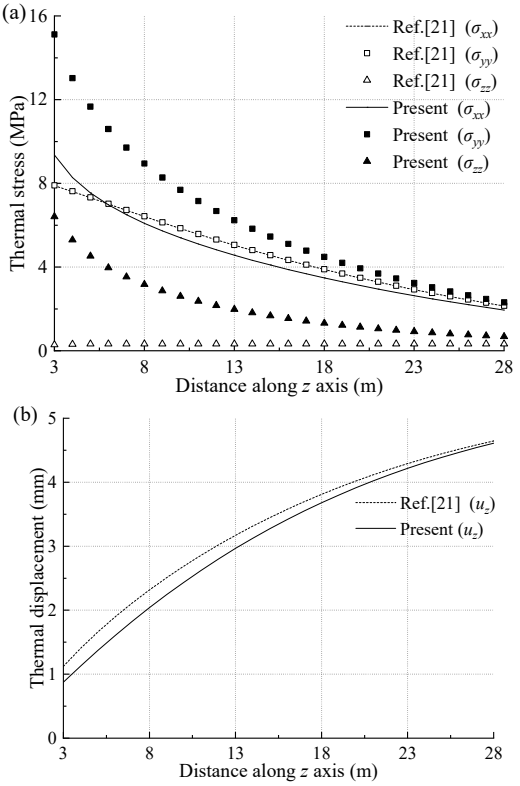

Fig. 3. Comparison of the thermal effects along line $\bar{L}$:(a) Thermal stress; (b) Vertical displacement.

4.3 Thermal effects at the examination points

Six points in Fig.2 are chosen as examination points. Their coordinates and thermal effects are listed in Table 2 and shown in Fig.4, respectively.

Table 2. Coordinates of the examination points

Point	Coordinates	Point	Coordinates
A_1	(24,1.975,500)	A_2	(24,1.975,300)
B_1	(480,1.975,500)	B_2	(480,1.975,300)
C_1	(480,500,500)	C_2	(480,500,300)

Fig.4a shows the variation of horizontal stress σ_{xx} with time. Although the stresses at points B_2 and C_2 are tensile before the 80th year, their values are below 0.1 MPa. By contrast, the stresses at other four points are compressive. Among these points, the peak of compressive stress at point A_1 is the largest and exists during the 40th ~ 70th year with a value of 15.2MPa.

Fig.4b illustrates the evolution of horizontal stress σ_{yy} with time. Before the 100th year, the stresses at points A_2, B_2 and C_2 are tensile and less than 0.5MPa. In contrast, the stresses at other three points are compressive. The maximum of compressive stress peaks at these points is 21.5MPa occurring in the 20th year at point A_1.

Fig.4c describes the change of vertical stress σ_{zz} with time. The tensile stress at point B_1 increases to the maximum of 1.0MPa in the 5th year and becomes into

compressive after the 50th year. Before the 70th year, the stress at point C_1 is tensile and less than 0.5MPa. By comparison, the stresses at other points are compressive. Among these points, the compressive stress at point A_1 is the largest having two peaks. The first peak is 9.4MPa in the 3th year and the other is 5.3MPa in the 700th year.

The shear stresses at points A_1, A_2, B_1 and B_2 are nearly zero because these points close the symmetrical location in the repository. Fig.4d only plots the development of shear stresses with time at points C_1 and C_2. The shear stress at point C_1 increases to the maximum of 2.1MPa in the 50th year. The tangential stress at point C_2 is lower than 1.0MPa during the sealing period.

Fig.4e displays the variation of horizontal displacement u_x with time. The order of the largest displacement at the interest points is $B_1 > B_2 > C_1 > C_2 > A_1 > A_2$. The horizontal displacement at point B_1 reaches to a maximum of 32mm in the 600th year.

Fig.4f portrays the evolution of displacement with time in *y*- and *z*-direction. Analogy with the shear stresses, the displacements in these two directions at points A_1, B_1 and the vertical one at point C_1 are nearly zero. The horizontal displacement at point C_1 increases to the maximum of 21mm in the 800th year. In terms of the vertical displacement, the peaks are 33mm at point A_2 in the 500th year, 19mm at point B_2 in the 600th year and 11mm at point C_2 in the 700th year, respectively.

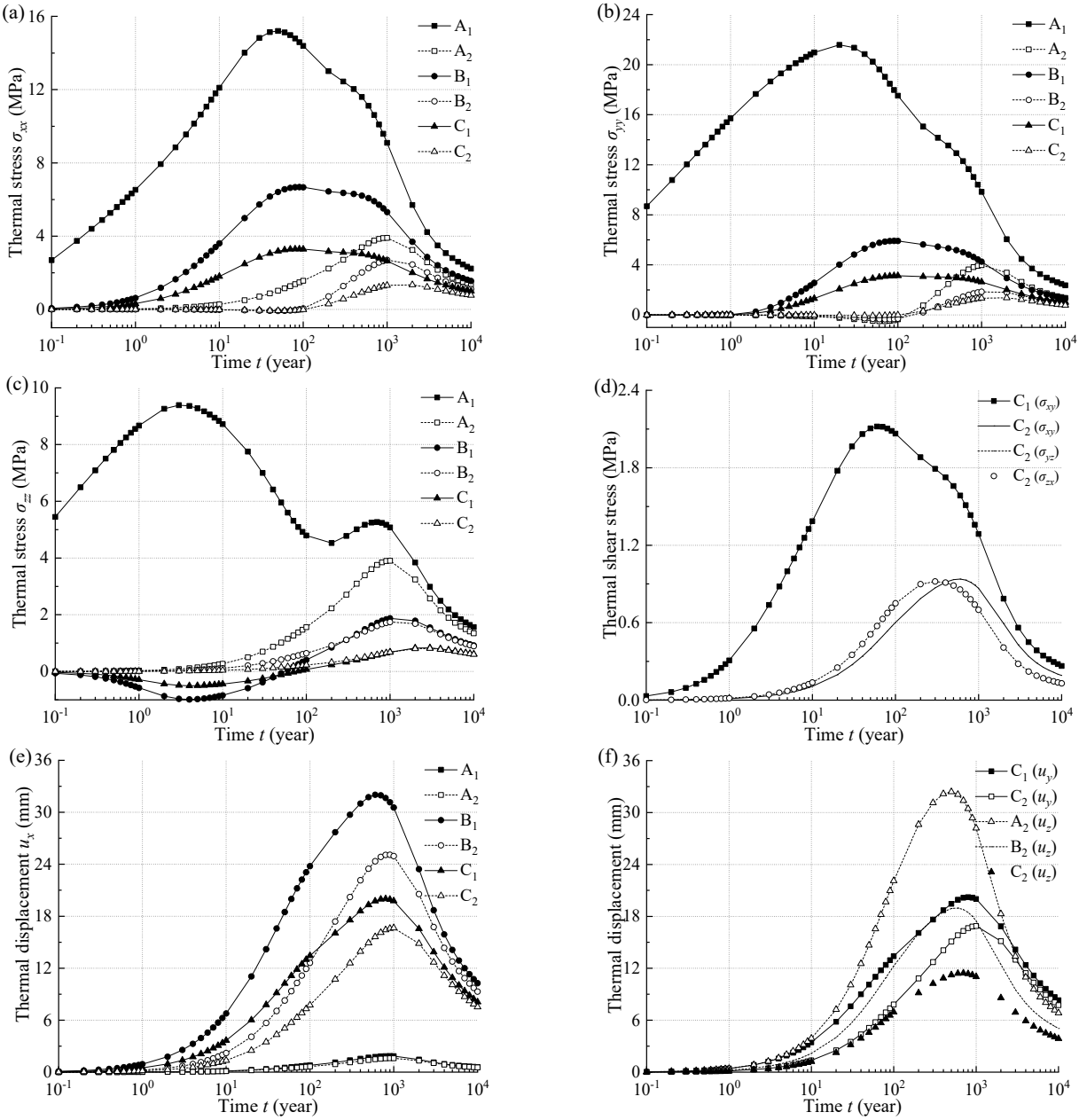

Fig.4. Thermal stresses and displacements at interest points.

4.4 Thermal effects on the examination plane

The present model is employed to investigate the thermal effects on the quarter of the disposal region plane(Plane

E) shown in Fig.2. The thermal stress and displacement after 10 years of sealing are illustrated in Fig.5. The spatial differences of the thermo-mechanical effects are significant. In the vicinity of the central pit, the compressive thermal stress of 20 MPa occurs. Howerver, the tensile thermal stress of 1 MPa exists between adjacent drifts. Large shear stress of 2 MPa mainly occurs at the repository corner. There are large deformation near the repository boundary.

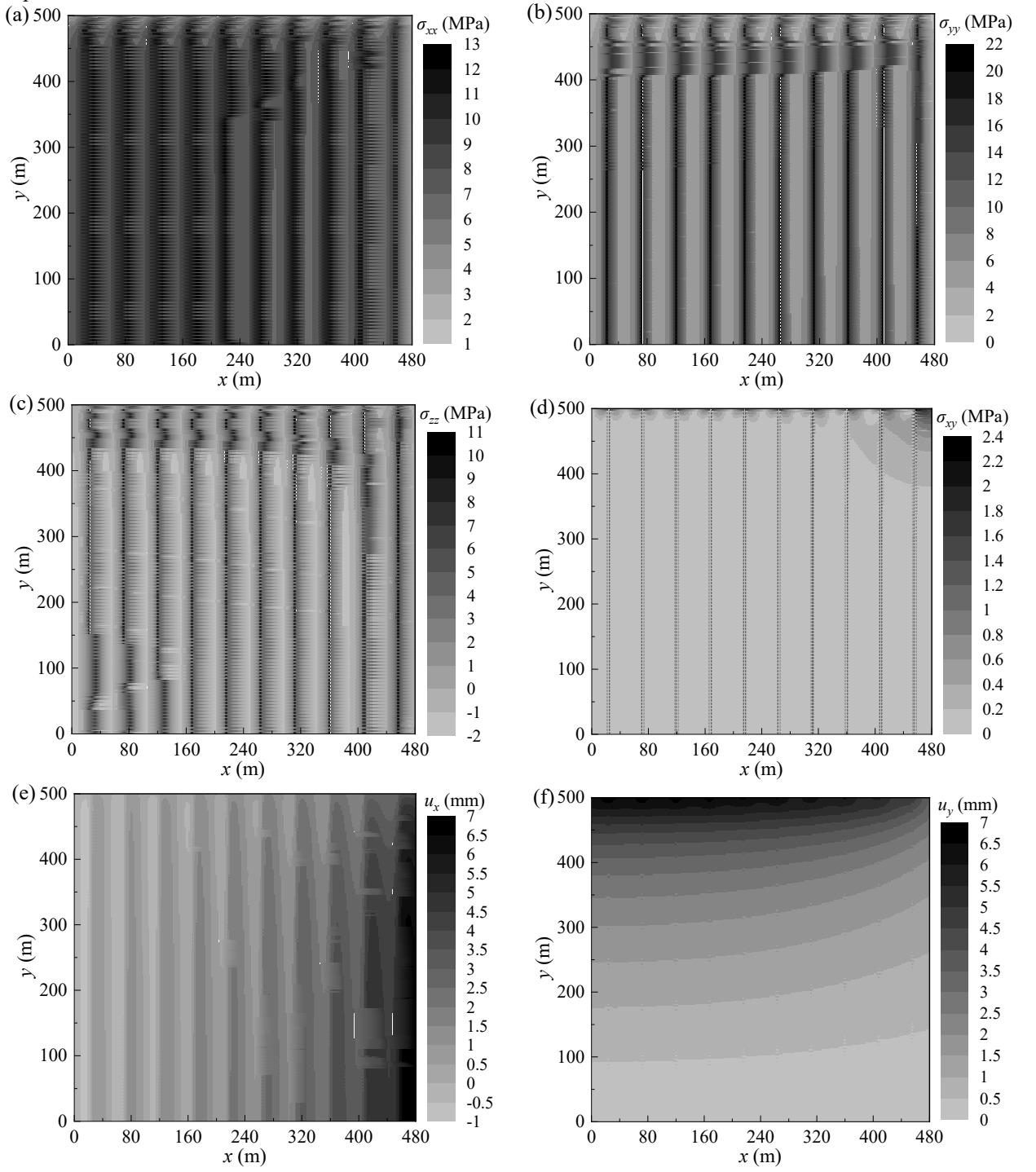

Fig. 6. Thermal stress and displacement on the quarter of the repository region plane after 10 years of closure.

4.5 Influences of pit/drift spacing on the thermal effects

For constant heat power per unit disposal area, the values of $d \times D$ in three schemes are set as 4 m × 60 m (S_1), 5 m × 48 m (S_2) and 6 m × 40 m (S_3), respectively. Fig.8 illustrates the thermal stress of point A_1 in these scenarios. The thermal stress at point A_1 increases with the enlargement of pit spacing and decrease of drift spacing.

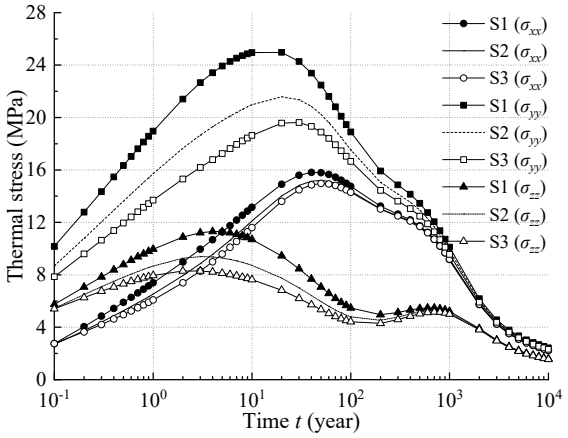

Fig. 8. Thermal stress at point A_1 of the three senarios.

5 Summary

To analyze the thermo-mechanical response of a repersitory, the thermal loadings are characterized as distributed decaying line heat sources, an image method in combination with a numerical integration scheme was developed. The results from several hypothetical calculation examples demonstrate that

(1) The presented method is efficient to calculate the effects of the thermal loading pattern and the burial depth of a geological repository on the thermal stress-displacement in the host rock.

(2) Due to the decay of the heat from the nuclear waste, the thermal stresses and displacements in the host rock increase at first and then decrease with time.

(3) The spatial differences of the thermo-mechanical effects are significant. Large thermal shear stress, tensile stress, and deformation occur at the repository corner, between adjacent drifts, and at the repository boundary, respectively.

(4) For a prescribed thermal loading, it is more efficient to mitigate the thermo-mechanical effects through enlarging the pit spacing than increasing the drift spacing.

Acknowledgement

This research was supported by the National Natural Science Foundation of China (Grant No.5137055) and Fundamental Research Funds for China Central University (Grant No. 2018YJS104).

References

1. J. Wang, L. Chen, R. Su, X.G. Zhao, Journal of Rock Mechanics and Geotechnical Engineering **10**, 411-435(2018).
2. J. Selroos, S. Follin, Hydrogeol. J. **22**, 1229-1232 (2014).
3. S.D. Ali, J. Kim, Ann. Nucl. Energy **101**, 301-311(2017).
4. M. Lönnqvist, H. Hökmark, Rock Mech. Rock Eng. **49**, 1123-1142(2016).
5. X.H. He, T. Ahn, J.P. Gwo, Corrosion **74**, 158-168 (2018).
6. W. Kim, K. Koh, S. Bae, J. Choi, Nucl. Eng. Technol. **40**, 3-9(2008).
7. S.Y. Yang, H.D. Yeh, J. Hazard. Mater. **169**, 108-112(2009).
8. Y.J. Kwon, Nucl. Sci. Eng. **164**, 264-286(2010).
9. S. Kwon, W.J. Cho, J.O. Lee, Nucl. Eng. Technol. **45**, 41-52(2013).
10. J.Y. Lee, D.K. Cho, H.J. Choi, J.W. Choi, L.M. Wang, Prog. Nucl. Energy **53**, 361-367(2011).
11. A.K. Verma, P. Gautam, T.N. Singh, R.K. Bajpai, Arab. J. Geosci. **8**, 8027-8038(2015).
12. S. Amgad, A. Mohamed, S. Shu, Prog. Nucl. Energy **85**, 747-755 (2015).
13. R.P. Gou, Engineering Geology **218**, 50-62 (2017).
14. J.O. Lee, H. Choi, J.Y. Kim, Int. J. Heat Mass Tran. **115**, 192-204(2017).
15. M.J. Kim, S.R. Lee, S. Yoon, J.S. Jeon, M.S. Kim, Comput. Geotech. **104**, 109-117(2018).
16. M.J. Kim, S.R. Lee, J.S. Jeon, S. Yoon, Ann. Nucl. Energy **123**, 190-199(2019).
17. J. Sundberg, P. Back, R. Christiansson, H. Hökmark, M. Ländell, J. Wrafter, Int. J. Rock Mech. Min. **46**,1042-1054(2009).
18. H. Hökmark, J. Claesson, Eng. Geol. **81**, 353-364(2005).
19. J. Li, M.S. Yim, D.M. Neclis, Ann. Nucl. Energy **38**, 243-253(2011).
20. D. Holton, S. Myers, G. Carta, A. Hoch, M. Dickinson, N. Carr, Eng. Geol. **211**, 102-119(2016).
21. J. Claesson, T. Probert, Eng. Geol. **49**, 223-229(1998).
22. K.B. Min, J. Lee, O. Stephansson, Int. J. Rock Mech. Min. **61**, 275-288(2013).
23. Svensk Käränbrnslehantering, *Long-term safety for the final repository for spent nuclear fuel at Forsmark*, *main report of the SR-Site project* (Swedish Nuclear Fuel and Waste Management Company, Stockholm, 2011).
24. R.B. Hetnarski, R.M. Eslami, *Thermal Stress—Advanced Theory and Applications*(Springer, New York, 2009).
25. H.S. Carslaw, J.C. Jaeger, *Conduction of Heat in Solids*(Oxford University Press, Oxford, 1959).
26. G.F. Dargush, P.K. Banerjee, Int. J. Solids Struct. **26**, 199-216(1990).
27. R. Pohrt, Q. Li, Phys. Mesomech. **17**, 334-340(2014).
28. Y. Zhang, Y.Y. Xiang, Int. J. Numer. Anal. Met. **38**, 1149-1171(2014).